Picomolar zinc binding modulates formation of Bcl10-nucleating assemblies of the caspase recruitment domain (CARD) of CARD9

Received for publication, July 19, 2018, and in revised form, September 4, 2018 Published, Papers in Press, September 11, 2018, DOI 10.1074/jbc.RA118.004821

Michael J. Holliday[‡], Ryan Ferrao[§1], Gladys de Leon Boenig[§], Alberto Estevez[§], Elizabeth Helgason[‡], Alexis Rohou[§], Erin C. Dueber[‡2], and Wayne J. Fairbrother[‡3]

From the [‡]Early Discovery Biochemistry Department and [§]Structural Biology Department, Genentech, South San Francisco, California 94080

Edited by Wolfgang Peti

The caspase recruitment domain–containing protein 9 (CARD9)–B-cell lymphoma/leukemia 10 (Bcl10) signaling axis is activated in myeloid cells during the innate immune response to a variety of diverse pathogens. This signaling pathway requires a critical caspase recruitment domain (CARD)–CARD interaction between CARD9 and Bcl10 that promotes downstream activation of factors, including NF-κB and the mitogen-activated protein kinase (MAPK) p38. Despite these insights, CARD9 remains structurally uncharacterized, and little mechanistic understanding of its regulation exists. We unexpectedly found here that the CARD in CARD9 binds to Zn^{2+} with picomolar affinity—a concentration comparable with the levels of readily accessible Zn^{2+} in the cytosol. NMR solution structures of the CARD9–CARD in the apo and Zn^{2+}-bound states revealed that Zn^{2+} has little effect on the ground-state structure of the CARD; yet the stability of the domain increased considerably upon Zn^{2+} binding, with a concomitant reduction in conformational flexibility. Moreover, Zn^{2+} binding inhibited polymerization of the CARD9–CARD into helical assemblies. Here, we also present a 20-Å resolution negative-stain EM (NS-EM) structure of these filamentous assemblies and show that they adopt a similar helical symmetry as reported previously for filaments of the Bcl10 CARD. Using both bulk assays and direct NS-EM visualization, we further show that the CARD9–CARD assemblies can directly template and thereby nucleate Bcl10 polymerization, a capacity considered critical to propagation of the CARD9–Bcl10 signaling cascade. Our findings indicate that CARD9 is a potential target of Zn^{2+}-mediated signaling that affects Bcl10 polymerization in innate immune responses.

During fungal infection, fungus-specific carbohydrates bind the C-type lectin receptors in myeloid cells, including Dectin-1, Dectin-2, and Mincle (1–3). These receptors engage, via an intercellular immunoreceptor tyrosine-based activation motif (ITAM)[4]-like motif or an adaptor protein containing an ITAM-like motif, Syk kinase. Syk, in turn, phosphorylates and activates protein kinase Cδ leading to subsequent phosphorylation and activation of the scaffolding protein CARD9 (caspase recruitment domain–containing protein 9) (4, 5). Upon activation, CARD9 recruits, via its N-terminal CARD, the CARD-containing Bcl10 (B-cell lymphoma/leukemia 10) and subsequently MALT1 to form the myeloid CARD9–Bcl10–MALT1 (CBM) signalosome. Upon complex formation, the CBM signalosome initiates the downstream activation of NF-κB required to mount an antifungal immune response (4, 6). Consistent with the critical and nonredundant role of CARD9 in this pathway, individuals deficient in CARD9 are highly susceptible to chronic fungal infections (7–10). CARD9 has also been shown to contribute to other nonfungal innate immune responses, such as cytosolic DNA sensing with Rad50 (11), intracellular bacterial infections through interaction with NOD2 (12), and viral RNA detection through association with RIG-I (13). The CARD9 signaling axis is implicated in a number of inflammatory diseases, including a genetic association with susceptibility to inflammatory bowel disease (14, 15), development of autoimmune disease of the eye (16), and progression of cardiovascular disease brought on by high-fat diet–induced obesity (17). Indeed, Wang *et al.* (18) observed that the activation of p38 MAPK by the CARD9–Bcl10 signaling axis induces obesity-

The authors declare that they have no conflicts of interest with the contents of this article.

This article contains Figs. S1–S7.

The atomic coordinates and structure factors (codes 6E25, 6E26, 6E27, and 6E28) have been deposited in the Protein Data Bank (http://wwpdb.org/).

Chemical shifts for the apo- and Zn^{2+}-bound CARD9–CARD monomer were deposited in the Biological Magnetic Resonance Database under BMRB accession numbers 30491 and 30492, respectively.

Electron microscopy density map for the CARD9–CARD filament has been deposited in the Electron Microscopy Data Bank under EMDB accession number 8976.

[1] Present address: Structural Chemistry Dept., Gilead Sciences, Foster City, CA 94404.

[2] To whom correspondence may be addressed: Early Discovery Biochemistry Dept., Genentech, 1 DNA Way, South San Francisco, CA 94080. Tel.: 650-225-3490; E-mail: dueber.erin@gene.com.

[3] To whom correspondence may be addressed: Early Discovery Biochemistry Dept., Genentech, 1 DNA Way, South San Francisco, CA 94080. Tel.: 650-225-6372; E-mail: fairbrother.wayne@gene.com.

[4] The abbreviations used are: ITAM, immunoreceptor tyrosine-based activation motif; CARD, caspase recruitment domain; ORCH, obesity-related cardiac hypertrophy; NS-EM, negative stain–electron microscopy; HSQC, heteronuclear signal quantum coherence; SOFAST-HMQC; selective optimized flip-angle short-transient heteronuclear multiple quantum coherence; CI, confidence interval; HDX, hydrogen-deuterium exchange; TEV, tobacco etch virus; IPTG, isopropyl 1-thio-β-D-galactopyranoside; RMSD, root mean square deviation; TCEP, tris(2-carboxyethyl)phosphine; PDB, Protein Data Bank; FP, fluorescence polarization; Ni-NTA, nickel-nitrilotriacetic acid; MAPK, mitogen-activated protein kinase; MBP, maltose-binding protein; CTF, contrast transfer function.

related cardiac hypertrophy (ORCH) in mice maintained on a high-fat diet. They further found that Zn^{2+} modulates ORCH development in this context, with Zn^{2+} deficiency aggravating and Zn^{2+} supplementation mitigating disease severity in a Bcl10-dependent manner (18). These findings fit within a larger body of literature indicating that Zn^{2+} acts as a signaling molecule in a number of immune cell types, wherein transient increases in cytosolic Zn^{2+}, known as Zn^{2+}-waves, serve to activate downstream signaling pathways (19–22). In general, however, the targets of the Zn^{2+}-wave and mechanisms by which Zn^{2+} impacts signaling remain poorly understood. Similarly, despite the broad importance of CARD9, CARD9 itself has remained structurally uncharacterized, and a mechanistic understanding of its regulation is lacking.

CARD9 comprises an N-terminal CARD followed by a "coiled-coil" domain of ~450 amino acids containing multiple distinct regions predicted to have high coiled-coil propensity. The CARD is critical for CARD9's recruitment of Bcl10, and by homology to CARD9's closest paralogue, CARD11 (CARD11, caspase recruitment domain–containing protein 11; also known as CARMA1), the CARD9–CARD is thought to act in a templating manner by forming a helical assembly able to potentiate the subsequent polymerization of Bcl10 required for signal propagation (6, 23). We therefore hypothesize that CARD9 signaling may be regulated by modulating the accessibility of its CARD and/or its propensity to generate a helical template. To better understand molecular mechanisms underlying CARD9 function, we determined the NMR solution structure of the CARD9–CARD, and we found, surprisingly, that it binds to Zn^{2+}, exhibiting a dissociation constant comparable with estimates of the "free" cytosolic Zn^{2+} concentration. Although the ground-state structure of the CARD9–CARD is essentially identical in the apo and Zn^{2+}-bound states, Zn^{2+} binding strongly stabilizes the fold and reduces conformational "breathing" of the helices. Upon overexpression in *Escherichia coli*, the CARD9–CARD is also capable of forming an extensively domain-swapped dimer, with interconversion of the CARD monomer and dimer strongly inhibited by Zn^{2+} binding. Furthermore, Zn^{2+} binding inhibits formation of helical filaments by the CARD9–CARD monomer that otherwise spontaneously assembles *in vitro*. A 20-Å negative-stain EM (NS-EM) structure of these filaments reported here demonstrates that they adopt a similar symmetry as the Bcl10–CARD helical assembly. Finally, we show through both a bulk assay and direct NS-EM visualization that the CARD9–CARD helical assembly is capable of directly templating Bcl10 polymerization.

Results

The CARD9–CARD binds Zn^{2+}

We purified ^{15}N-labeled CARD9–CARD (residues 2–97) using a cleavable affinity tag and size-exclusion chromatography (see under "Experimental procedures"). A ^{15}N HSQC NMR spectrum of the resulting monomeric CARD exhibits significant peak dispersion, suggesting that the domain adopts a well-folded structure. We determined near-complete backbone and side-chain assignments for the CARD and calculated a solution structure with a backbone RMSD of 0.7 Å (RMSD calculated for structured residues 10–97, see Table 1 for complete statistics). The CARD9–CARD adopts a canonical death-domain structure containing six antiparallel α-helices with 9 N-terminal residues remaining largely unstructured. As shown in Fig. 1*A*, the CARD9–CARD aligns well with the crystal structure of its closest paralogue, the human CARD11–CARD (1.9-Å backbone RMSD to PDB code 4LWD (23)), including the conserved kink in the α1 helix common among CARDs. The largest differences between the CARD9 and CARD11–CARDs are apparent in α-helices α3 and α4 and the flexible α3–α4 loop, a region with high *B*-factors in the CARD11–CARD structure and also comprising the largest sequence divergence between the CARDs.

Given the role of Zn^{2+} in modulating ORCH and the central role of CARD9 in this pathology (18), we tested whether the CARD9–CARD itself interacts with Zn^{2+}. The ^{15}N HSQC NMR spectrum of the CARD is significantly perturbed upon addition of 1:0.5 or 1:1 concentrations of $ZnCl_2$, with all shifted peaks in the slow-exchange limit, suggesting that the CARD binds Zn^{2+} with sub-micromolar affinity (Fig. 1*B*). Further increasing the Zn^{2+} concentration above a 1:1 ratio minimally affects the spectrum, indicating that the CARD9–CARD con-

Table 1
Structural statistics for the NMR assignments and solution structures of the apo and Zn^{2+}-bound monomeric CARD9–CARD

	Apo CARD	Zn^{2+}-bound CARD
PDB code	6E26	6E25
BMRB code	30492	30491
Assignments (%)[a]	89 (97)	81 (77)
^{1}H	91 (97)	90 (97)
^{13}C	91 (98)	72 (49)
^{15}N	76 (96)	75 (95)
NOE restraints	1509	1592
Intra-residue ($i = j$)	423	407
Sequential ($\|i - j\| = 1$)	410	421
Medium range ($\|i - j\| <5$)	395	444
Long range ($\|i - j\| \geq 5$)	281	320
NOE constraints per restrained residue[b]	15.9	16.8
Hydrogen bond constraints	66	60
Long range ($\|i - j\| \geq 5$)	0	0
Dihedral angle constraints	140	140
Total no. of restricting constraints	1715	1792
Restricting constraints per restrained residue[b]	18.1	18.9
Long range ($\|i - j\| \geq 5$)	3.0	3.4
Total structures computed	100	100
No. of structures included	20	20
Distance violations per structure		
0.1–0.2 Å	9.0	6.4
0.2–0.5 Å	2.0	1.25
>0.5 Å	0	0
RMS of distance violation/constraint (Å)	0.02	0.02
Maximum distance violation (Å)	0.47	0.46
Dihedral angle violations per structure		
1–10°	4.1	2.55
>10°	0	0
RMS of dihedral angle violation per constraint (°)	0.52	0.33
Maximum dihedral angle violation (°)	7.1	4.6
RMSD[c]		
Backbone	0.7 (1.8)	0.5 (1.5)
Heavy atoms	1.2 (2.2)	1.0 (1.9)
Ramachandran[d]		
Most favored (%)	93.6	94.9
Additionally allowed (%)	6.4	5.0
Generously allowed (%)	0	0.1
Disallowed	0	0

[a] Total assignment completeness, with backbone completeness reported in parentheses.
[b] Residues 3–97 contain conformational restraining constraints.
[c] Residues 10–97 reported, with all-residue RMSDs reported in parentheses.
[d] Residues 10–97, calculated with Procheck.

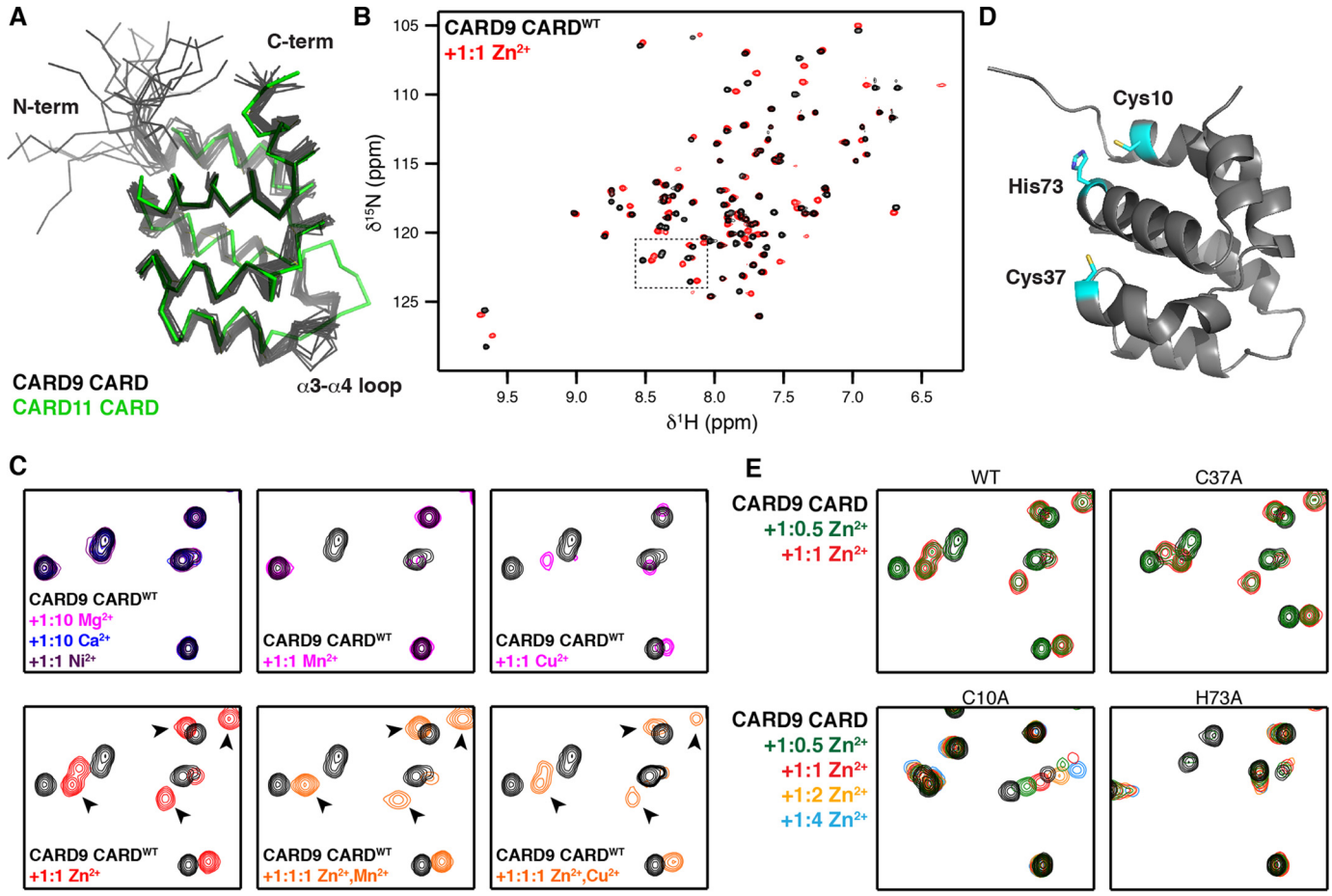

Figure 1. CARD9–CARD binds Zn^{2+}. *A,* ribbon diagram of the 20 lowest energy structures calculated for the apo-CARD9–CARD (*black*), aligned with the crystal structure of the CARD11–CARD (PDB code 4I16, *green*). *B,* ^{15}N HSQC spectra of the CARD9–CARD in the absence (*black*) and presence (*red*) of equimolar $ZnCl_2$. *Dashed line box* indicates region expanded in *C* and *E*. *C, top row*, selected region of CARD9–CARD^{WT} ^{15}N HSQC spectra apo or with equimolar $CaCl_2$, $MgCl_2$, $NiCl_2$, $MnCl_2$, or $CuCl_2$. *Bottom row*, selected region of CARD9–CARD^{WT} ^{15}N HSQC spectra apo or with equimolar $ZnCl_2$, equimolar $ZnCl_2$ and $MnCl_2$, or equimolar $ZnCl_2$ and $CuCl_2$. *Arrowheads* indicate examples of peak positions unique to the Zn^{2+}-bound state. *D,* lowest energy CARD9–CARD structure with the potential Zn^{2+}-coordinating residues highlighted in *cyan*. *E,* selected region of CARD9–CARD^{WT} and CARD9–CARD^{C37A} ^{15}N HSQC spectra with 1:0 (*black*), 1:0.5 (*green*), and 1:1 (*red*) $ZnCl_2$, demonstrating slow exchange dynamics. CARD9–CARD^{C10A} and CARD9–CARD^{H73A} are shown with 1:0 (*black*), 1:0.5 (*green*), 1:1 (*red*), 1:2 (*orange*), and 1:4 (*blue*) $ZnCl_2$, demonstrating a shift to the intermediate-to-fast exchange regime.

tains a single high-affinity metal-binding site (Fig. S1). To determine whether this binding is specific for Zn^{2+}, we incubated the CARD9–CARD with other divalent metal ions. No chemical shift changes are observed upon addition of 1:10 molar concentrations of either $CaCl_2$ or $MgCl_2$, indicating that the CARD is unable to bind Ca^{2+} or Mg^{2+} (Fig. 1*C*). A stoichiometric concentration of $NiCl_2$ likewise induces no chemical shift changes in the CARD9–CARD. However, Mn^{2+} and Cu^{2+} do interact with the CARD9–CARD at stoichiometric concentrations, with Cu^{2+} inducing chemical shift changes and the paramagnetic Mn^{2+} inducing enhanced relaxation of a number of peaks (Fig. 1*C*). Upon simultaneous addition of Zn^{2+} and Mn^{2+} to the CARD9–CARD in a 1:1:1 ratio, the peak signature indicates that all of the CARD is Zn^{2+}-bound, with remaining peak disappearances attributable to secondary Mn^{2+} interactions outside the Zn^{2+}-binding site (Fig. 1*C*, see *arrows* indicating peaks unique to the Zn^{2+}-bound CARD9–CARD). Simultaneous addition of stoichiometric concentrations of Cu^{2+} and Zn^{2+} results in populations of the CARD9–CARD bound to each of the two metals, shown by the presence of peaks corresponding to both the Cu^{2+}-bound and Zn^{2+}-bound states. The Zn^{2+}-bound peaks are ~50% less intense than when Zn^{2+} is added alone (Fig. 1*C*, *arrowheads*), indicating approximately equal affinity of the CARD for Zn^{2+} and Cu^{2+}. These findings are consistent with the relative affinities expected by the Irving–Williams series (24). The concentration of labile cytosolic copper has proven difficult to measure with high accuracy, although estimates suggest that it is in the femtomolar range or lower (25, 26). Because the CARD9–CARD dissociation constant for Zn^{2+} (and therefore for Cu^{2+}) is several orders of magnitude larger than the typical cytosolic Cu^{2+} concentration, but comparable with estimates of the "free" cytosolic Zn^{2+} concentration (see below), we suggest that Zn^{2+} is likely to be a physiological ligand for CARD9, but depending on the cellular context, Cu^{2+} binding could play a role as well. We thus proceeded to characterize Zn^{2+} binding to the CARD9–CARD.

Cysteine and histidine residues typically mediate Zn^{2+} coordination, with additional binding often provided by glutamate and aspartate side chains. To determine which residues in the CARD9–CARD are responsible for Zn^{2+} coordination, we generated alanine substitutions at either of the two cysteines (CARD^{C10A} or CARD^{C37A}) or the sole histidine (CARD^{H73A}),

the positions of which are depicted in Fig. 1*D*. Although CARD^{C37A} continues to bind Zn^{2+} in the slow-exchange limit, both CARD^{C10A} and CARD^{H73A} shift binding to the intermediate-to-fast exchange regime, indicating a significant reduction in affinity and demonstrating that Cys-10 and His-73 are involved in coordinating Zn^{2+} (Fig. 1*E*). The only glutamates or aspartates potentially in position to provide additional Zn^{2+} coordination are a stretch of acidic residues (Glu-5, Asp-7, Asp-8, and Glu-9) on the unstructured N-terminal region of the CARD9–CARD. Upon mutation of Glu-5 or Glu-9 to Gln, we found no substantial differences in the Zn^{2+}-bound spectrum, indicating no contribution to coordination. In contrast, we found that the Zn^{2+}-bound spectrum of CARD^{D7N} differs substantially from CARD^{WT}, despite the binding remaining in the slow-exchange regime (Fig. S2). These data suggest that Asp-7 is less critical than Cys-10 or His-73 for Zn^{2+} affinity but that coordination by Asp-7 results in conformational changes to the CARD. CARD^{D8N} exhibits subtler Zn^{2+}-bound ^{15}N HSQC differences as compared with CARD^{WT}, comprising reduced line-broadening of the binding-site–proximal amide peaks Cys-10, Trp-11 (backbone and side chain), Ser-12, and Gln-69 (side chain), suggesting a role for Asp-8 in coordination as well (Fig. S2).

The CARD9–CARD exhibits a picomolar dissociation constant for Zn^{2+}

Zn^{2+} binding to the CARD9–CARD is sufficiently tight to preclude direct affinity determination by NMR titration. We instead utilized competition against the fluorescent Zn^{2+}-binding dye mag-fura-2, which has a dissociation constant of 20 nM for Zn^{2+} (27). As shown in Fig. 2*A*, the CARD9–CARD competes effectively against mag-fura-2, although less effectively than EDTA (K_D of $\sim 10^{-16}$ for Zn^{2+}). Fitting these data to the exact competitive binding equation described by Wang (28), CARD^{WT} binds Zn^{2+} with a dissociation constant of 0.73 nM (95% confidence interval (CI) 0.45–1.07 nM). Consistent with the NMR data, CARD^{C10A} and CARD^{H73A} are unable to compete with mag-fura-2, whereas CARD^{C37A} binds with comparable affinity to CARD^{WT}. The mutations D7N and D8N each decrease binding affinity ~2–3–fold, whereas the double mutant CARD$^{D7N/D8N}$ exhibits an ~25-fold decrease, suggesting that the two acidic residues may trade-off responsibility for coordinating the Zn^{2+} ion (Fig. 2*C*). Because the measured picomolar affinity of the CARD9–CARD is approaching the lower limit accessible in competition with the 20 nM mag-fura-2, we additionally assessed affinity among the tightly binding constructs in competition with the more tightly binding indo-1 dye (K_D for Zn^{2+} of 0.16 nM (29)). As shown in Fig. 2, *B* and *C*, affinities as measured in competition with indo-1 agree with those determined with mag-fura-2, confirming that the CARD9–CARD binds Zn^{2+} with a picomolar dissociation constant, comparable with estimates of the free cytosolic Zn^{2+} concentration.

Zn^{2+} binding does not significantly alter the CARD9–CARD structure

Given the high affinity and specificity that the CARD9–CARD exhibits for Zn^{2+}, we were curious as to the impact of

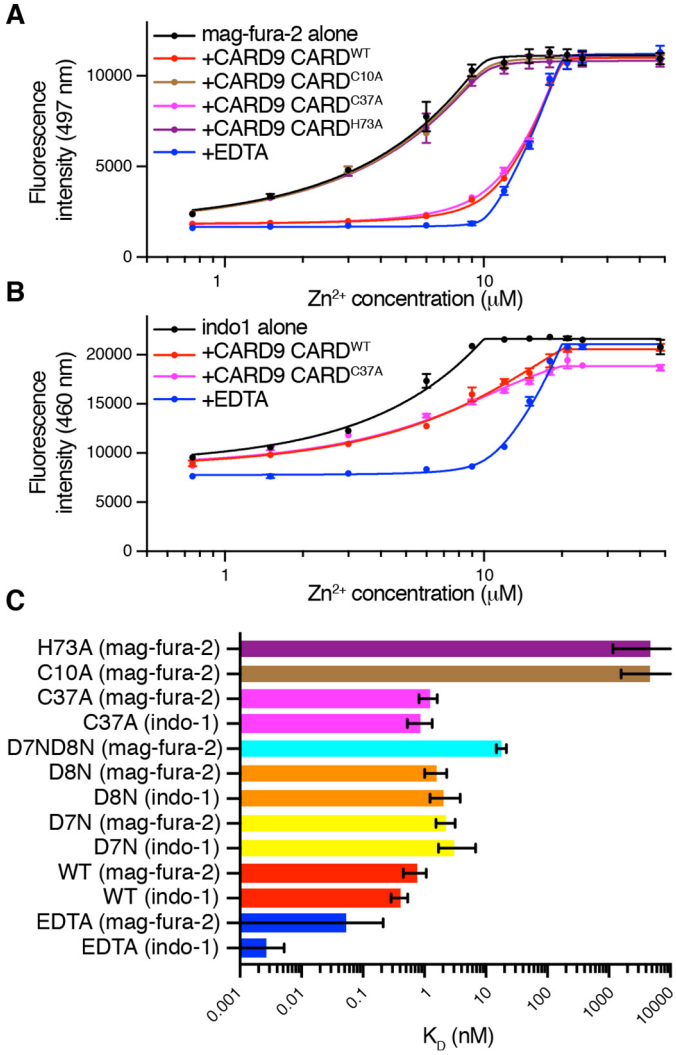

Figure 2. The CARD9–CARD binds Zn^{2+} with a picomolar dissociation constant. Representative competition binding curves are shown for CARD9–CARD^{WT}, CARD9–CARD mutants, or EDTA against mag-fura-2 (*A*) or indo-1 (*B*). *Error bars* represent the standard deviation of three technical replicates. *Solid lines* represent best fits to the generalized competition equation described by Wang (28). *C*, dissociation constants determined via competition against either mag-fura-2 or indo-1 as indicated. *Error bars* represent asymmetric profile likelihood 95% CI. For H73A and C10A, no upper limit was found for the 95% CI. For EDTA, either in competition with mag-fura-2 or indo-1, no lower limit was found for the 95% CI.

Zn^{2+} binding on the CARD structure. We thus determined near-complete backbone and side-chain chemical shift assignments for the Zn^{2+}-bound CARD9–CARD and calculated the NMR solution structure to a backbone RMSD value of 0.5 Å (RMSD calculated for structured residues 10–97, see Table 1 for complete statistics).

In the Zn^{2+}-bound structure, the Zn^{2+} ion forms a bridge between Cys-10 at the beginning of α1 and His-73 at the beginning of α5 (Fig. 3*A*). Because of the ambiguity in coordination by Asp-7 and Asp-8, we only imposed constraints to maintain coordination by Cys-10 and His-73 during structure calculations. Although full quantum mechanical calculations were not performed, Asp-7 interacts with the Zn^{2+} ion with one or both carboxyl oxygens in all of the 20 lowest energy structures, consistent with its prominent role in coordination (representative structures shown in Fig. 3*A*). The apo and Zn^{2+}-bound struc-

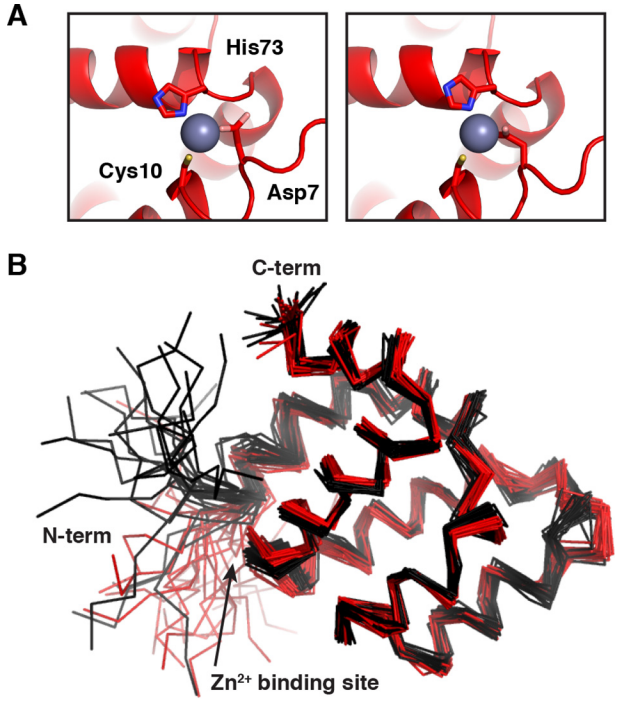

Figure 3. Solution structure of the CARD9–CARD in the Zn^{2+}-bound state. *A,* two lowest energy Zn^{2+}-bound CARD9–CARD structures, demonstrating Zn^{2+} coordination by Cys-10, His-73, and Asp-7. *B,* alignment of the 20 lowest energy structures of the CARD9–CARD in the apo (*black*) and Zn^{2+}-bound (*red*) states.

tures are remarkably similar, with a backbone RMSD (residues 10–97) of 0.95 Å, which is only slightly higher than the RMSD of the apo state itself (Fig. 3*B*). We further manually compared the NOESY spectra of the CARD in the apo and Zn^{2+}-bound states in search of more subtle differences in the structures. Although the specific NOE cross-peaks used in the two calculations vary somewhat due to differential peak overlap and line-broadening between the apo and Zn^{2+}-bound states, we were unable to conclusively identify any instances in which an NOE cross-peak was present in one state and not the other. We therefore conclude that Zn^{2+} binding does not significantly alter the ground-state solution structure of the CARD9–CARD.

Zn^{2+} binding stabilizes the CARD9–CARD and inhibits α-helical unraveling

Although binding of a Zn^{2+} ion to the CARD9–CARD does not substantially alter its ground-state structure, we were curious as to the potential impact of Zn^{2+} binding on the CARD stability and conformational dynamics. We monitored denaturation of the CARD9–CARD monomer via differential scanning fluorimetry and found that addition of Zn^{2+} increases the thermostability of the CARD by nearly 14 °C, reflecting a substantial stabilization of the domain upon Zn^{2+} binding (Fig. 4*A*).

To monitor conformational stability, we performed an NMR-based hydrogen-deuterium exchange (HDX) experiment to monitor the solvent accessibility of backbone amides in the apo and Zn^{2+}-bound states. Aqueous ^{15}N-labeled CARD9–CARD was lyophilized and then resuspended in 99.99% D_2O, followed by a collection of a series of SOFAST-

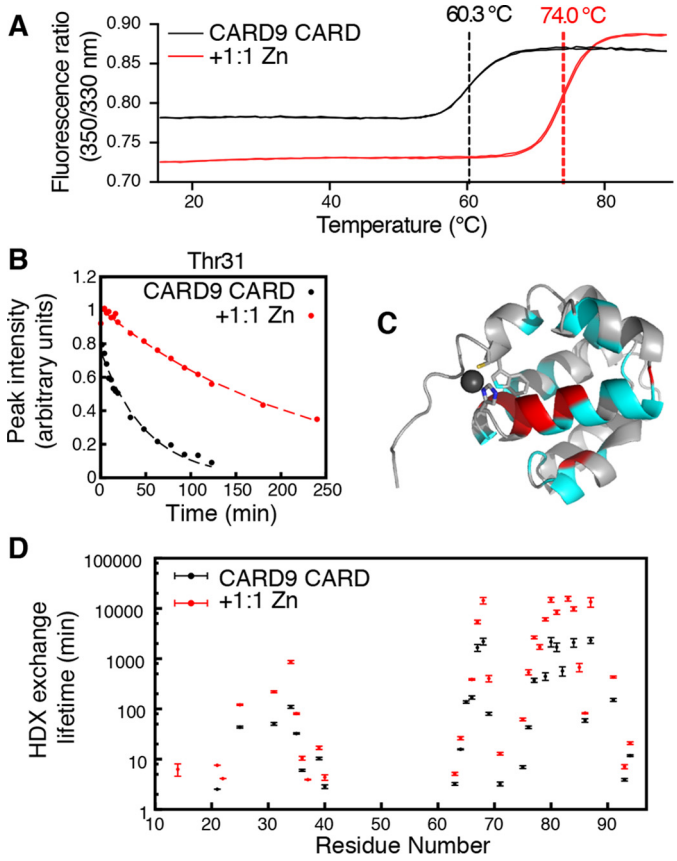

Figure 4. Zn^{2+} binding stabilizes the CARD9–CARD and slows HDX. *A,* differential scanning fluorimetry melt curve for apo (*black*) and Zn^{2+}-bound (*red*) CARD9–CARD. Inflection points are indicated by *dashed vertical lines*. Two technical replicates are shown for each condition, which agreed to within 0.1 °C of the mean values shown on the *graph*. *B,* representative NMR HDX peak-height decay curve for Thr-31 in the absence (*black*) and presence (*red*) of equimolar Zn^{2+}. *Circles* represent ^{15}N-SOFAST-HMQC peak intensities, and *dotted lines* are best-fit single exponential decay curves. *C,* CARD9–CARD, lowest energy Zn^{2+}-bound solution structure. Residues for which Zn^{2+} binding increased the HDX lifetime, which includes all observed peaks, are colored *cyan*. The indole amide of Trp-11 also exhibits enhanced protection and is colored *cyan*. Those residues for which lifetimes could be calculated in both the apo and Zn^{2+}-bound states and were increased greater than 5-fold by Zn^{2+} binding are colored *red*. *D,* global CARD9–CARD backbone amide HDX exchange lifetimes in the absence (*black*) and presence (*red*) of equimolar $ZnCl_2$. *Error bars* represent profile likelihood 95% confidence intervals. Residues are excluded for which no signal remained at the first time point or for which overlap precluded accurate peak height determination.

HMQC experiments, which allow for rapid data collection. Approximately 35% of residues remain at least partially protonated by the first 1.5-min time point. For all residues that we were able to monitor, the HDX lifetime was significantly increased in the context of Zn^{2+} binding, with half-lives increasing by 1.5–14–fold over the apo state (Fig. 4, *B* and *D*). The residues most strongly protected by Zn^{2+} binding map predominantly to helices α4 and α5, which lie on either side of His-73 (Fig. 4*C*). These data demonstrate that Zn^{2+} binding locks the CARD in a more stable compact conformation, with less conformational breathing in the helices than in the apo state.

The CARD9–CARD can adopt a domain-swapped dimeric structure

Upon recombinant overexpression of the CARD9–CARD in *E. coli* and subsequent purification, two distinct species can be

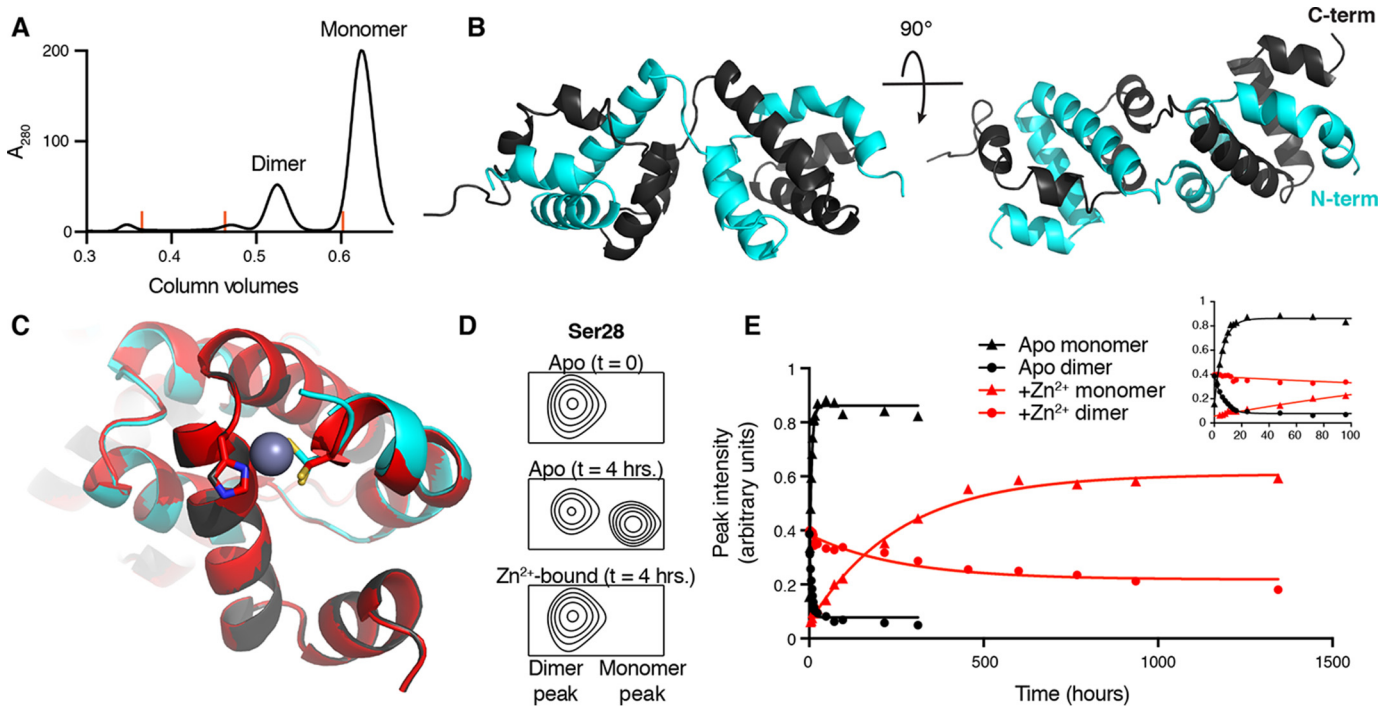

Figure 5. The CARD9–CARD can adopt a 3-helix domain-swapped dimer in solution. *A,* size-exclusion chromatography UV trace (280 nm), demonstrating the presence of both monomeric and dimeric CARD9–CARD when purified from *E. coli*. *Orange lines* indicate peak positions of molecular mass standards of 158, 44, and 17 kDa. *B,* crystal structure of the domain-swapped dimer, with the two polypeptide chains colored in *gray* or *cyan*. *C,* alignment of the apo (*gray/cyan*) and Zn^{2+}-bound (*red*) domain-swapped dimer structures with Cys-10 and His-73 depicted as *sticks*. Cys-10 in the apo-form adopts two distinct rotameric states in the crystal structure, both of which are depicted. *D,* ^{15}N-SOFAST-HMQC spectra, beginning with 100% CARD9–CARD dimer, focused on the representative backbone amide peak of Ser-28, immediately (*top*) and 4 h (*middle*, without Zn^{2+}, *bottom*, with Zn^{2+}) after beginning incubation at 25 °C. See Fig. S3*C* for full spectra. *E,* Ser-28 monomer (*triangles*) and dimer (*circles*) peak heights as a function of time in the apo (*black*) or Zn^{2+}-bound (*red*) states. *Inset* plot includes only the first 100 h of the experiment, allowing visualization of the exponential approach to equilibrium in the apo state.

isolated: the monomeric CARD for which NMR structures are shown in Fig. 4, and a kinetically stable dimeric state that accounts for ~20% of the purified protein at the final gel filtration step (Fig. 5*A*). We determined the 1.36-Å resolution X-ray crystal structure of this CARD9–CARD dimer (see Table 2 for complete statistics) using molecular replacement with the CARD11–CARD structure (PDB code 4LWD). The dimer is composed of two six-helix bundles, each of which aligns well to the CARD9–CARD monomer (Fig. S3*A*). Each bundle, however, contains three helices from each of the two polypeptide chains, forming a domain-swapped dimer with a short linker crossing over between helices α3 and α4 (Figs. 5*B* and Fig. S3*B*).

The Zn^{2+}-binding site in the CARD9–CARD is distal from the strand swap between α3 and α4, such that the domain swap would not be expected to alter Zn^{2+} binding. Consistent with this expectation, NMR chemical shift changes upon addition of Zn^{2+} to the dimer are nearly identical to those seen for the monomeric state. We thus soaked Zn^{2+} into domain-swapped dimer crystals, identified a single condition where Zn^{2+} occupies one of the two binding sites, and solved the crystal structure at a resolution of 1.81 Å (see Table 2 for complete statistics). The Zn^{2+} ion binds where expected based on our NMR structure of the Zn^{2+}-bound monomer, with clear electron density demonstrating its coordination by both Cys-10 and His-73 (Fig. 5*C* and Fig. S3*B*). Additional electron density is present, which suggests Zn^{2+} coordination by a third residue in the N-terminal tail; however, the residues N-terminal of Asp-9

Table 2
Structural statistics for the CARD9 CARD apo and Zn^{2+}-bound domain-swapped dimer crystal structures

	Apo CARD dimer	Zn^{2+}-bound CARD dimer
PDB code	6E28	6E27
Wavelength	1.000	1.000
Space group	P 1 2_1 1	P 1 2_1 1
Cell dimensions		
a, *b*, *c* (Å)	43.98 37.43 56.88	44.01 37.46 56.96
α, β, γ (°)	90 101.47 90	90 101.79 90
Resolution range (Å)	37.94–1.36 (1.41–1.36)	43.08–1.81 (1.88–1.81)
R_{merge} (%)	3.905 (84.11)	7.536 (120)
$I/\sigma I$	21.67 (1.71)	14.06 (1.37)
$CC_{1/2}$	0.999 (0.715)	0.999 (0.540)
Completeness (%)	95.72 (73.23)	98.24 (95.65)
Redundancy	6.3 (5.2)	6.6 (6.6)
Resolution (Å)	1.36	1.81
Unique reflections	37,560 (2849)	16,495 (1582)
R_{work}/R_{free} (%)	0.1797 / 0.1937	0.2066 / 0.2577
Non-hydrogen atoms		
Protein	1524	1498
Ligands	0	1
Water	153	89
Average *B*-factor (Å^2)		
Protein	36.48	44.78
Ion		63.81
Water	41.34	45.46
RMSD		
Bond length (A)	0.009	0.011
Bond angles (°)	1.01	1.05
Ramachandran		
Favored (%)	99.45	98.89
Allowed (%)	0.55	1.11
Outliers (%)	0	0

are too poorly resolved to conclusively identify which (likely Asp-7 or Asp-8) is participating in the coordination, likely reflecting conformational heterogeneity in the coordination throughout the crystal. In agreement with the minimal ground-state differences observed between the apo and Zn^{2+}-bound monomeric structures, no notable structural changes are observed in the domain-swapped dimer upon Zn^{2+} binding (Fig. 5*C*).

The domain-swapped dimer exhibits a similar ^{15}N HSQC spectrum as the monomer, but with distinct differences, especially for those residues near the strand swap. By monitoring a single amide peak (Ser-28, Fig. 5*D*) with resolvable monomeric and dimeric chemical shifts, we were able to track the kinetics of interconversion of the two states. At 25 °C, we found that the dimer and monomer interconvert with a half-life of 4.1 h (95% CI 3.8–5.4 h) in the absence of Zn^{2+}. This interconversion is dramatically slowed, however, in the presence of Zn^{2+}, where the dimer exhibits a half-life of 179 h (95% CI 155–206 h), representing a nearly 50-fold decrease in interconversion rate (Fig. 5*E*). There additionally appears to be a shift in the monomer–dimer equilibrium, with ~3-fold more dimer present at equilibrium in the presence of Zn^{2+} relative to the apo state. These findings are consistent with the HDX data, suggesting that the presence of Zn^{2+} locks the CARD9–CARD in a more stable conformation, preventing helical unraveling that must be required for the monomeric and domain-swapped dimeric conformations to interconvert.

We observed that the homologous CARD11–CARD (50% identity to the CARD9–CARD) is also capable of adopting a relatively long-lived dimeric conformation upon overexpression in *E. coli*, with an *in vitro* half-life of 34 min (95% CI 28–48 min) at 25 °C (Fig. S4, *A–C*). We were unable to conclusively demonstrate that the CARD11–CARD adopts a homologous domain-swapped dimeric structure as the CARD9–CARD, but the long half-life and a comparable extent of chemical shift changes intimate a similar structure. Upon addition of stoichiometric $ZnCl_2$ to the ^{15}N-labeled CARD11–CARD monomer, we observed no significant NMR chemical shift perturbations, indicating that Zn^{2+} binding is not conserved within the protein family (Fig. S4*D*).

The CARD9–CARD forms in vitro filaments in a Zn^{2+}-regulated manner

In the absence of Zn^{2+}, we found that upon concentrating monomeric CARD9–CARD above ~150 μM, the solution became cloudy. We visualized this opaque solution by NS-EM and observed that the CARD9–CARD monomer assembles into long filaments with a diameter of ~90 Å (Fig. 6*A*). To monitor the effect of Zn^{2+} binding on these filaments, we purified the CARD9–CARD monomer bound to a stoichiometric amount of Zn^{2+} by adding a saturating concentration of $ZnCl_2$ prior to a final gel-filtration column. In contrast to the apo CARD, we found that at 200 μM the Zn^{2+}-bound CARD remained clear by eye and filament-free as monitored by NS-EM (Fig. 6*B*). Addition of EDTA to chelate the Zn^{2+} away from the CARDs leads to formation of filaments within ~10 min at 25 °C. We monitored filament formation though UV absorbance at 350 nm and found that they form readily at 200 and 150 μM, but minimally at 100 μM (Fig. 6*C*). Doubling the salt concentration to 300 mM also effectively blocks CARD9–CARD polymerization at these protein concentrations, a property that permitted NMR data collection and structure determination of the apo CARD9–CARD monomer described above (Fig. 1*A*). These assemblies are readily reversible upon re-binding of Zn^{2+}, as addition of Zn^{2+} stoichiometrically equal to the EDTA concentration induces disassembly within ~5 min. Unlike the monomeric CARD9–CARD, the domain-swapped CARD9–CARD dimer solution remains clear at concentrations of >2 mM, irrespective of the presence of Zn^{2+}, indicating that the dimeric state of the CARD is unable to form filaments.

We found that Zn^{2+} binding inhibits filament assembly of the CARD9–CARD monomer but does not block it entirely. Upon concentrating the Zn^{2+}-bound CARD9–CARD solution to ~800 μM, it also becomes cloudy, and filaments can be observed by NS-EM (Fig. S5*A*). These filaments are ~180 Å in diameter and appear to be tandem assemblies of two filaments, as they often end ~90 Å wide, off-center "tails." After addition of Zn^{2+} to the single-width filaments induced by Zn^{2+} depletion (as depicted in Fig. 6, *A* and *C*), we found that all single-width filaments had disassembled when visualized by NS-EM, whereas a small population (undetectable by UV absorbance, Fig. 6*C*) of tandem filaments had formed, presumably from a subset of filaments that had been able to bind Zn^{2+} and adopt a stabilized tandem conformation prior to disassembly (Fig. S5*A*). In the context of the full CARD9 protein, the coiled-coil domain would necessarily protrude from any helical CARD assembly, likely blocking side-mediated interactions of the filaments. We therefore anticipate that these observed tandem CARD9–CARD filaments are likely an *in vitro* artifact. Nonetheless, the vast majority of filaments rapidly disassemble in the presence of Zn^{2+}, demonstrating that Zn^{2+} binding regulates the stability of CARD9–CARD helical assemblies.

CARD9–CARD filaments comprise a similar helical assembly as Bcl10 and are able to template Bcl10 nucleation

Because CARD9 is thought to propagate signaling via nucleation of Bcl10 helical assemblies, we wondered whether these *in vitro* filaments are representative of the helical template that seeds Bcl10 polymerization. To determine whether the filaments adopt a conformation consistent with this nucleating capacity, we determined an ~20-Å resolution NS-EM structure of the CARD9–CARD filaments (Fig. 6*D*, *left*). The CARD9–CARD filaments are 90 Å in diameter and form a hollow helical assembly with a 5-Å rise and 102° rotation, which are nearly identical to the 5.0-Å rise and 100.8° rotation determined previously for the Bcl10–CARD helical assembly (30). Direct comparison of low-resolution NS-EM structures of the CARD9–CARD and Bcl10–CARD assemblies (Fig. 6*D*, *right*) (EMD-5729 (23)) demonstrates that although the slight differences in helical symmetry lead to discernable differences over several turns of the helix, the two CARDs adopt highly similar filamentous structures. Although the Bcl10 CARD contains an extended C-terminal helix that enables unambiguous fitting of the CARD monomers into the filament structure, the CARD9–CARD contains no such large asymmetry, preventing us from independently placing our CARD monomeric structure con-

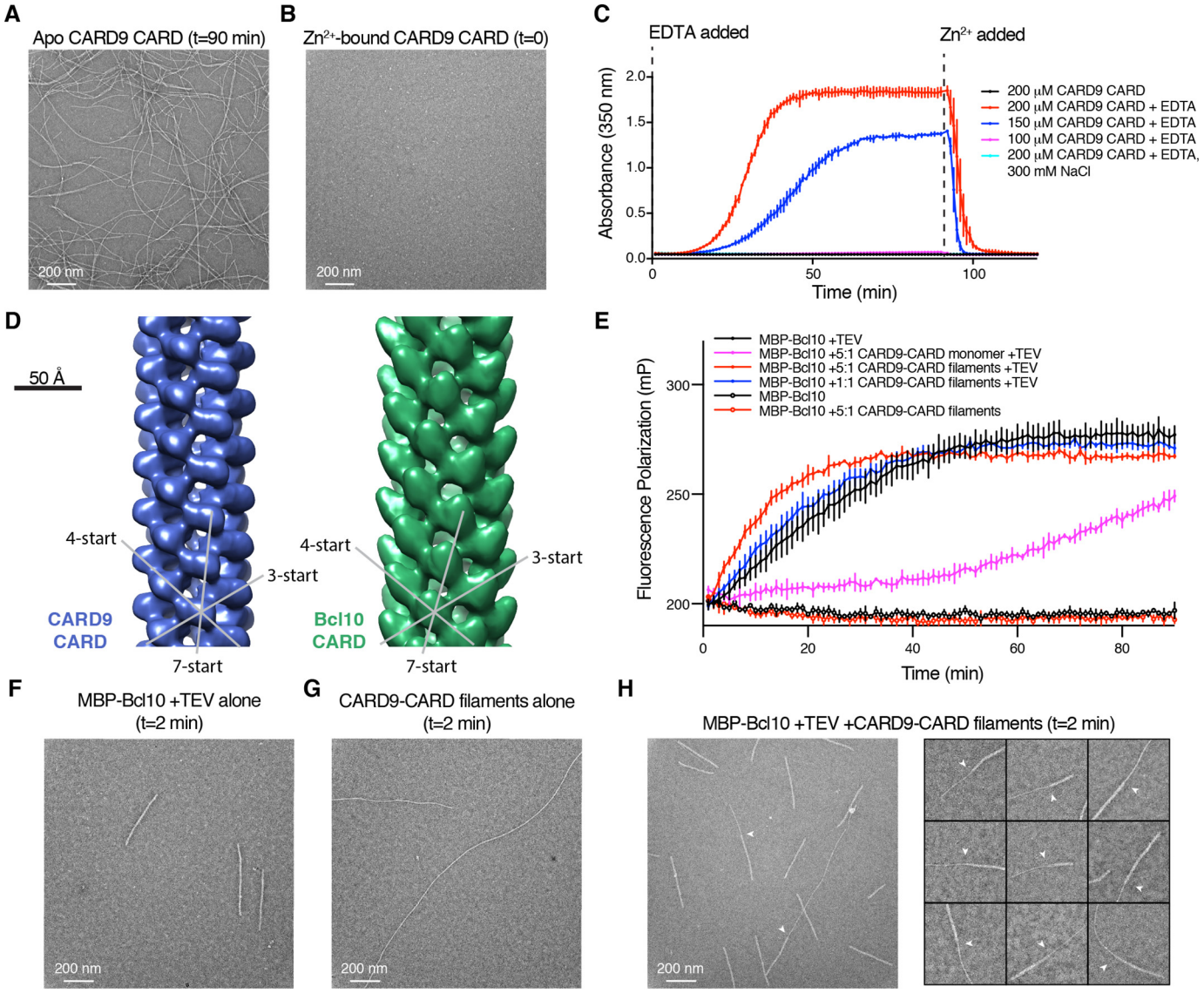

Figure 6. The CARD9–CARD forms filaments in a Zn^{2+}-regulated manner that are capable of directly templating the Bcl10 helical assembly. *A,* CARD9–CARD filaments, visualized by NS-EM. Filaments were generated as in *C*, *red line*, with NS-EM samples prepared at 90 min. *B,* NS-EM micrograph of 200 μM CARD9–CARD saturated with 1:1 Zn^{2+}, sample taken just before EDTA addition in *C*. *C,* CARD9–CARD filament assembly, monitored by absorbance at 350 nm. All samples contain CARD9–CARD saturated with 1:1 Zn^{2+} and 150 mM NaCl (except as indicated); at $t = 0$, 250 μM EDTA was added to the indicated samples. At 90 min, 250 μM $ZnCl_2$ was added to all samples. *Error bars* represent the standard deviation of three technical replicates. *D, left,* 20-Å resolution NS-EM reconstruction of the CARD9–CARD helical assembly; *right,* 20-Å resolution NS-EM–derived Bcl10–CARD helical assembly solved by Qiao *et al.* (23) (EMD-5729). The dominant 3-, 4-, and 7-start helical symmetries are indicated, highlighting the similarity between the structures. *E,* fluorescence polarization assay utilizing 2 μM MBP–Bcl10 sparsely tagged with Alexa Fluor 488 dye. At time $t = 0$, TEV protease, CARD9–CARD monomer, and/or CARD9–CARD filaments were added as indicated. *Error bars* represent the standard deviation of three technical replicates. *F–H,* NS-EM micrograph of Bcl10 filaments alone (*F*), CARD9–CARD filaments alone (*G*), or CARD9–CARD filament-nucleated Bcl10 filaments (*H*) generated under identical conditions as in *E* (5:1 ratio, *red*), 2 min after addition of TEV protease. *H*, *white arrows* indicate CARD9–CARD-to-Bcl10 transitions.

clusively into the EM density. However, given the similarity of the helical symmetry between the assemblies, we predict that a higher resolution CARD9–CARD structure would reveal an orientation comparable with the Bcl10–CARD filament. The CARD9–CARD filaments are thus consistent in structure with what we would expect in a templating assembly.

To directly monitor the capacity for the CARD9–CARD filaments to nucleate Bcl10, we adapted a fluorescence polarization (FP)-based Bcl10 nucleation assay described by Qiao *et al.* (23). Briefly, a Bcl10 construct was generated linked N-terminally to MBP via a TEV protease-cleavable linker; this MBP tag was shown to block *in vitro* Bcl10 polymerization, which otherwise occurs rapidly for either the full-length Bcl10 or the Bcl10 CARD alone. Bcl10 was also sparsely labeled with Alexa Fluor 488 dye prior to a final gel-filtration column. Bcl10 polymerization is induced by addition of TEV protease, which removes >50% of the MBP in under 2 min and nearly all MBP within 10 min, irrespective of the presence of CARD9–CARD (Fig. S5*B*). Subsequent Bcl10 polymerization is then monitored by the change in FP corresponding to the increased molecular weight of the filament.

As shown in Fig. 6*E*, addition of CARD9–CARD filaments to MBP–Bcl10 at a 5:1 molar ratio accelerates the formation of Bcl10 filaments relative to Bcl10 alone, although the addi-

tion of monomeric CARD9–CARD slows Bcl10 polymerization significantly, presumably by competing with Bcl10 homotypic binding sites. We additionally performed a replicate of the experiment utilizing an independent preparation of the CARD9–CARD filaments and purification of MBP–Bcl10. As shown in Fig. S5*C*, we observed nearly identical results with an identical replicate (2 μM MBP–Bcl10) and additionally found comparable CARD9–CARD-induced acceleration utilizing a lower concentration of 1 μM MBP–Bcl10.

The capacity for the CARD9–CARD filaments to accelerate bulk Bcl10 polymerization could stem either from direct CARD–CARD templating wherein the Bcl10–CARD helical assembly extends continuously from the CARD9–CARD assembly or from indirect effects, *e.g.* increasing local Bcl10 concentration. To distinguish these possibilities, we visualized CARD9–CARD filament-nucleated Bcl10 filaments shortly (2 min) after addition of TEV protease by NS-EM. Because Bcl10 contains a C-terminal Ser/Thr-rich domain in addition to its CARD, its filaments are appreciably wider than the CARD9–CARD filaments (Fig. 6, *F* and *G*). As shown in Fig. 6*H* for the nucleated sample, we were able to readily identify continuous filaments comprising regions of both CARD9–CARD and Bcl10, demonstrating direct CARD9–CARD-templated nucleation of the Bcl10 helical assembly. We were unable to find any instance of more than a single CARD9–Bcl10 transition within a given filament, suggesting that nucleation, like Bcl10 filament extension (30), is unidirectional.

Discussion

Although total eukaryotic cellular Zn^{2+} concentrations are typically hundreds of micromolar, the vast majority of it is sequestered by tight interactions with proteins (31). Indeed, ~10% of the human proteome has been estimated to bind Zn^{2+} in structural, catalytic, or regulatory capacities (32). Considerable effort has been made to address the challenging question of what concentration of free Zn^{2+} is readily available in the cytosol of eukaryotic cells, with estimates ranging from 5 pM to 1.67 nM (33, 34); however, over diverse cell types and detection methods, most studies have measured concentrations in the range of 0.1–1 nM (35–40). Structural binding sites (*e.g.* zinc finger domains) typically bind Zn^{2+} with dissociation constants much lower than the free or readily available cytosolic Zn^{2+} concentration, and therefore, they remain saturated under all conditions. In contrast, regulatory binding sites typically bind with dissociation constants comparable with the picomolar cytosolic Zn^{2+} concentration, such that fluctuations in local Zn^{2+} concentration can modulate function via changes to the Zn^{2+}-bound status of a given protein (31).

The immune system modulates Zn^{2+} concentrations from the organismal to the subcellular levels over time scales of seconds to hours in response to diverse stimuli (21, 22, 41). Within immune cells, several stimuli have been shown to induce a Zn^{2+}-wave wherein cellular stores of Zn^{2+} are released on the order of minutes after signal initiation, acting as a second messenger; these include stimulation of IgE in mast cells that activate MAPK, extracellular signal-regulated kinase (ERK), and c-Jun N-terminal kinase (JNK) signaling (20) and activation of monocytes by a range of stimuli, including lipopolysaccharide, inducing downstream NF-κB and MAPK signaling (19). Generally, the mechanism of Zn^{2+} release and the targets of increased cytosolic Zn^{2+} remain unknown. Specific to CARD9 signaling, Wang *et al.* (18) demonstrated that Zn^{2+} deficiency exacerbates cardiac hypertrophy in response to diet-induced obesity and that the onset of disease and an observed Zn^{2+}-mediated rescue depend on the activation of p38 MAPK by the CARD9–Bcl10 signaling axis.

Here, we have demonstrated that the CARD9–CARD specifically binds to Zn^{2+} with picomolar affinity, akin to proteins that utilize Zn^{2+} in a regulatory role; the *in vitro* affinity suggests a regulatory role for Zn^{2+} binding to CARD9; however, further characterization will be required to determine to what extent the cellular context influences the binding of Zn^{2+} to the CARD9–CARD. To our knowledge, this is the first observation of metal binding in the CARD family or the larger death-domain family. Among the close paralogues to CARD9 (CARD11, CARD10, and CARD14), the coordinating cysteine and histidine are not conserved (Fig. S7*A*), consistent with the lack of Zn^{2+} binding observed for the CARD11–CARD (Fig. S4*D*). The histidine and cysteine are conserved within CARD9 orthologues among mammals but not in reptiles or more divergent species (Fig. S7*B*).

Although Zn^{2+} binding does not substantially alter the CARD9–CARD structure, it does increase its stability, reducing the conformational flexibility of the domain. Moreover, Zn^{2+} dramatically affects the polymerization propensity of the CARD9–CARD. Indeed, the most striking *in vitro* impact of Zn^{2+} binding that we observed was the modulation of filament formation, shown in Fig. 6, *A–C*. Although it has been assumed that CARD9, like CARD11, propagates signaling by forming a nucleating seed, Fig. 6 represents the first direct evidence that the CARD of CARD9 is capable of forming a helical assembly, that this assembly closely mirrors the symmetry of the Bcl10 helical assembly, and that the CARD is capable of directly templating Bcl10 polymerization. The micrometer length filaments shown in Fig. 6*A* were generated with high concentrations of a CARD9 construct lacking the coiled-coil region and are thus unlikely to reflect the size of CARD9 assemblies that would form in cells. Rather, we suggest a model wherein CARD9–CARDs are brought to a high local concentration by coiled-coil domain-mediated oligomerization, driving formation of a CARD9–CARD helical "seed" that acts to template and thereby nucleate assembly of Bcl10 filaments.

Given the role of Zn^{2+} in modulating this template formation, we predict that the primary role of Zn^{2+} binding in CARD9 will prove to be in modulating the propensity to form this template and hence propagate signaling. Within dendritic cells where CARD9 functions, cytosolic zinc concentrations have been shown to decrease during maturation, potentially serving to prime the CARD9–CARD for subsequent signaling events (42). Alternatively, a "Zn^{2+}-wave" type of transient Zn^{2+} increase could serve to blunt excessive signaling though CARD9 by promoting helical disassembly after stimuli. A detailed temporal study of zinc levels during maturation and stimulation will be required to tease out the specific mechanisms by which Zn^{2+} binding may modulate the CARD9 signaling axis.

The similarity between the NMR solution structures of the apo and Zn^{2+}-bound CARD9–CARD (Fig. 3) along with the dramatic differences in stability and conformational flexibility (Fig. 4) suggest that the CARD within the helical assembly may require conformational rearrangement as compared with the monomer in solution. This phenomenon was recently demonstrated for the Bcl10 CARD, for which significant structural rearrangement was observed in a 4-Å resolution cryo-EM structure of the helix as compared with the monomeric NMR solution structure (30). Indeed, the largest differences between the Bcl10–CARD structures are in the orientation of helix α1, which in the CARD9–CARD contains Cys-10 and would thus be conformationally restricted by Zn^{2+} binding. Unfortunately, as was reported for filaments of the Bcl10 CARD alone, CARD9–CARD filaments present primarily as single filaments on NS-EM grids but almost exclusively as massive bundles of filaments (approximately micrometer diameter) when imaging by cryo-EM is attempted. The presence of these large bundles may also help to explain the relatively weak bulk solution nucleating capacity of the CARD9–CARD filaments (Fig. 6*E*), as they necessarily sequester large numbers of unproductive CARDs. David *et al.* (30) were ultimately able to determine a cryo-EM structure of the Bcl10–CARD filament using a construct containing the Ser/Thr-rich domain that is disordered relative to the CARD core and therefore absent in the reconstruction. Nevertheless, the Ser/Thr-rich domains serve to block side-to-side filament associations and are observable *en masse* on each individual filament, allowing us to distinguish the Bcl10 filaments from the thinner CARD9–CARD filaments (30). A similar strategy in CARD9 may allow for future high-resolution structure determination, which would provide insight into both homotypic and heterotypic CARD–CARD interactions, as well as into the specific mechanism by which Zn^{2+} binding modulates CARD9–CARD helical assembly.

As is common in the death-domain family, the CARD9–CARD engages in interactions with other CARDs (Fig. 6, *D* and *H*), generating helical assemblies in which the individual domains share a common orientation relative to the helical axis (43). The symmetric nature of the domain-swapped dimer would interfere with this assembly, explaining why the dimer is unable to incorporate into filaments. We thus speculate that the domain-swapped CARD9–CARD dimer (Fig. 5) may act as a negative regulator of CARD9 signaling that could be modulated by Zn^{2+} binding. The domain-swapped structure, however, is formed between CARD9–CARDs under the high concentrations of *E. coli* overexpression and outside of the context of the full proteins. Further characterization of the full-length protein under physiological conditions, perhaps by utilizing conformationally specific antibodies or an engineered protein deficient in domain swapping, will be required to determine whether the domain-swapped conformation is indeed biologically relevant.

In conclusion, we have identified and structurally characterized multiple conformations accessible to the CARD9–CARD, including a monomer, a domain-swapped dimer, and a filamentous helical assembly (graphically summarized in Fig. 7). CARD9 binds to Zn^{2+} with picomolar affinity, which modulates interconversion between these states, stabilizing the CARD9–CARD ground-state conformation and restricting its capacity to form Bcl10-nucleating filaments. We have thus identified CARD9 as a potential target of Zn^{2+}-mediated signaling during innate immune responses.

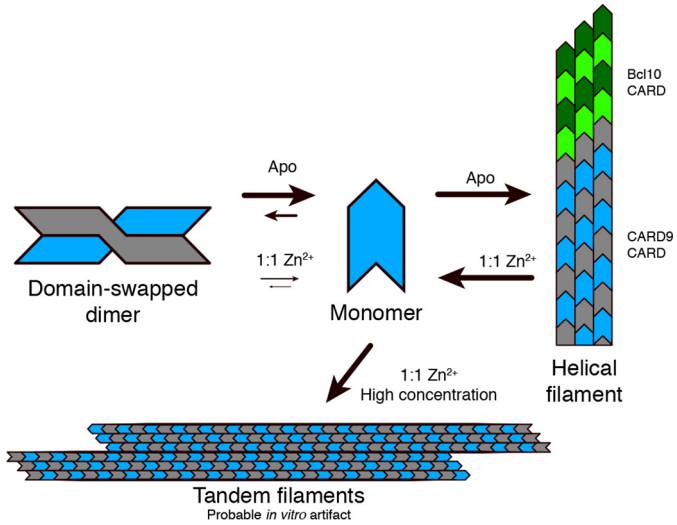

Figure 7. Cartoon depiction of the observed conformational states of the CARD9–CARD. CARD9–CARDs are depicted in *gray* and *blue* with *arrows* qualitatively indicating the impact of Zn^2 binding on the various transitions. Bcl10 CARDs are depicted in *green*.

Experimental procedures

Protein purification

CARD9 and CARD11–CARDs (residues 2–97 for CARD9 and 8–109 for CARD11) were expressed in BL21(DE3) cells with an N-terminal, TEV protease-cleavable His_6 tag. Protein production was achieved by growth for 48–72 h at 16 °C in TB autoinduction media or ^{15}N autoinduction media for unlabeled and ^{15}N-labeled protein, respectively (44). ^{13}C,^{15}N-Labeled protein was generated by induction in ^{13}C,^{15}N minimal media with 0.5 mM IPTG for 6 h at 37 °C. Proteins were purified by Ni-NTA (Qiagen), overnight cleavage by TEV protease, removal of imidazole by dialysis, and removal of TEV and any remaining uncleaved protein by Ni-NTA. Final purification and separation of monomeric and dimeric species were achieved via a Superdex 75 gel-filtration column (GE Healthcare). For all proteins used in metal-binding experiments, 5 mM EDTA was added prior to the final gel-filtration column. For proteins used in CARD9–CARD filament assays, 500 μM $ZnCl_2$ was added after the second Ni-NTA column, prior to concentration before the gel-filtration step.

For the Bcl10 FP assay, an *E. coli* expression construct was generated comprising an N-terminal His_6 tag followed by MBP, a TEV cleavage site, $Bcl10^{C29A/C10A}$, a short linker, and an HA peptide (MBP–Bcl10). The cysteines were mutated to allow for labeling exclusively on the Ser/Thr-rich domain and not the CARD. The ORF was designed to exactly replicate the construct generated by Qiao *et al.* (23), with the addition of GSGSYPYDVPDYA at the C terminus. MBP–Bcl10 was expressed in BL21(DE3) cells in LB media, which were induced by addition of 0.2 mM IPTG at A_{600} 0.7 for 1 h at 37 °C. MBP–Bcl10 was purified by Ni-NTA and eluted in ~3 ml, to which 2 μM Alexa Fluor 488 C_5 maleimide (ThermoFisher Scientific)

was added, followed by incubation for 10 min at room temperature. The labeled protein was then loaded directly with no concentration onto a Superdex 200 gel-filtration column (GE Healthcare) in 20 mM Tris, 150 mM NaCl, 0.5 mM TCEP, pH 7.5. Both the FP assay and preparation of grids for NS-EM were initiated within 2 h of the protein eluting from the gel-filtration column.

NMR assignments and solution structure determination

For apo assignments and structure determination, monomeric ^{13}C,^{15}N-labeled CARD9–CARD was purified in 50 mM Tris, 300 mM NaCl, 0.5 mM TCEP, pH 7.0, and concentrated to 400 μM for all NMR experiments. All experiments were collected at 37 °C on an 800-MHz Bruker spectrometer with a cryogenically cooled probe. Backbone assignments were determined through sequential assignments using ^{15}N HSQC, CBCA(CO)NH, HNCACB, HNCO, HN(CA)CO, and (H)CC(CO)NH experiments. Side-chain assignments were determined using ^{13}C HSQC (aliphatic and aromatic), HCCH-TOCSY, and ^{13}C NOESY-HSQC (aliphatic and aromatic, 150-ms mixing times) experiments. Additional ^{15}N NOESY-HSQC (150-ms mixing time) and ^{13}C NOESY-HSQC (aliphatic and aromatic, 150-ms mixing times, dissolved in 99.99% D_2O) experiments were collected to assist in structure determination.

For the Zn^{2+}-bound CARD9–CARD, monomeric ^{13}C,^{15}N-labeled CARD was purified as above to 400 μM followed by addition of 480 μM $ZnCl_2$. Backbone and side-chain assignments were transferred from the apo form, utilizing ^{15}N HSQC, HNCACB, HNCA, ^{13}C HSQC (aliphatic and aromatic), HCCH-TOCSY, and ^{13}C NOESY-HSQC (aliphatic and aromatic, 150 ms mixing times) experiments, with additional ^{15}N NOESY-HSQC (150-ms mixing time) and ^{13}C NOESY-HSQC (aliphatic and aromatic, 150 ms mixing times, dissolved in 99.99% D_2O) experiments collected to assist in structure determination. Stereospecific assignments for valine and leucine methyl groups were determined for the Zn^{2+}-bound CARD9–CARD by expressing the protein in M9 media with a 1:9 ^{13}C/^{12}C glucose ratio and collection of ^{13}C HSCQ spectra as described by Senn *et al.* (45); these stereospecific assignments were subsequently transferred to the spectra of the apo protein. All spectra were referenced directly (^1H) or indirectly (^{13}C and ^{15}N) to an internal 2,2-dimethyl-2-silapentane-5-sulfonic acid standard. All spectra were processed using Bruker TopSpin version 3.5 and subsequently analyzed in CcpNMR Analysis version 2.4 (46).

For both apo and Zn^{2+}-bound samples, a small proportion of the monomeric protein converted to the domain-swapped dimer over the course of extended NMR data collection; however, the concentration remained sufficiently low as to not register in the 3D experiments and was therefore ignored for both sequential assignments and structure calculation.

For structure determination of both the apo and Zn^{2+}-bound CARD9–CARD, dihedral angles were estimated using TALOS+ (47). For the Zn^{2+}-bound CARD, restraints were enforced to maintain coordination by Cys-10 Sγ and His-73 Nδ1. NOE peaks were assigned and initial structure determination was achieved using the CYANA version 3.97 NOE assignment and structure determination package (48, 49). Sum of r^{-6} averaging was used for all NOEs. For each round of CYANA NOE assignment and structure determination, 100 structures were generated, with the 20 lowest target function structures proceeding to the next round. After the final round of NOE assignments, 100 structures were calculated and subsequently refined in explicit water using the PARAM19 force field in CNS version 1.2 (50, 51) and the WaterRefCNS package developed by Dr. Robert Tejero. The 20 lowest energy structures for each of the apo and Zn^{2+}-bound refinements in water are presented here. Structures were evaluated using PROCHECK-NMR, with statistics presented in Table 1. All structural depictions were generated in PyMOL.

Metal binding by NMR

^{15}N HSQC spectra were collected on 100 μM ^{15}N-labeled WT and mutant CARD9–CARDs in 50 mM HEPES, 300 mM NaCl, 0.5 mM TCEP, pH 7.0, on a 600-MHz Bruker spectrometer at 37 °C, unless otherwise noted. ^{15}N-SOFAST HMQC spectra of 150 μM ^{15}N-labeled CARD11–CARD with or without 150 μM $ZnCl_2$ were collected in 50 mM HEPES, 300 mM NaCl, 0.5 mM TCEP, pH 7.0, on an 800-MHz Bruker spectrometer at 25 °C. Stock concentrations of $ZnCl_2$, $MnCl_2$, $CuCl_2$, and $NiCl_2$ were determined via inductively coupled plasma MS.

Metal competition assays

Competition assays were performed in 20-μl volumes in 10 mM HEPES, 150 mM NaCl, pH 7.5. Wildtype (WT) or mutant CARD9–CARDs were mixed 1:1 with either mag-fura-2 or indo-1 dyes, with final concentrations of 10 μM each. Stock CARD9–CARD concentrations were determined by measuring absorbance at 280 nm; mag-fura-2 and indo-1 stock concentrations were determined by measuring absorbance at 369 and 346 nm, respectively, in the presence of EDTA. CARD9–CARD and dye were incubated at 25 °C with the indicated concentrations of Zn^{2+} for 15 and 45 min for mag-fura-2 and indo-1, respectively, to ensure that measurements were made under equilibrium conditions. For mag-fura-2 samples, Zn^{2+} binding was monitored by measuring emission at 497 nm upon excitation at 325 nm. For indo-1 samples, Zn^{2+} binding was monitored by measuring emission at 460 nm upon excitation at 320 nm. All measurements were made on a Molecular Devices SpectraMax M5e plate reader. Data were fit to the exact competitive binding equation described by Wang (28) using GraphPad Prism 7.

Differential scanning fluorimetry

Protein denaturation was monitored by differential scanning fluorimetry using the NanoTemper Prometheus NT.48 for both data collection and analysis. 100 μM CARD9–CARD was prepared with or without addition of 100 μM $ZnCl_2$ in 50 mM HEPES, 150 mM NaCl, 0.5 mM TCEP, pH 7.5. Temperature was increased at 1 °C/min, and the protein-folding state was monitored via the ratio of tryptophan fluorescence at 350 and 330 nm. Melting temperature was determined as the inflection point of the 350/330 ratio.

Hydrogen-deuterium exchange

250 μM ^{15}N-labeled monomeric CARD9–CARD samples were generated in 50 mM HEPES, 300 mM NaCl, 250 μM $ZnCl_2$, 0.5 mM TCEP, pH 7.0, with or without 1 mM EDTA. Samples were lyophilized and resuspended in 99.99% D_2O, followed by immediate collection of ^{15}N-labeled SOFAST-HMQC (52) experiments at 25 °C on a Bruker 600-MHz spectrometer for time points shown. The mid-point of the SOFAST-HMQC experiments was used as the time points for both plotting and fitting. For all resolved peaks, peak height decay curves were fit to a single-phase exponential using GraphPad Prism 7.

Crystallography and structure determination

Dimeric WT CARD9–CARD was purified in 20 mM Tris, 150 mM NaCl, 0.5 mM TCEP, pH 7.0, and concentrated for crystallization. Apo crystals were generated by vapor diffusion at 19 °C in 0.4-μl sitting drops by mixing 20 mg/ml CARD9–CARD dimer and 1.1 M ammonium tartrate dibasic, pH 7.0 (Hampton Research), at a 1:1 ratio. Crystals were transferred into a cryoprotectant solution of the crystallization solution supplemented with 20% glycerol and frozen in liquid nitrogen. Crystals into which Zn^{2+} was soaked were generated by vapor diffusion at 19 °C in 0.4-μl sitting drops comprising a 1:1 mix of 20 mg/ml CARD9–CARD dimer and 5% v/v tacsimate, 0.1 M HEPES, pH 7.0, 10% w/v PEG monomethyl ether 5,000 (Hampton Research). These crystals were transferred into the crystallization buffer supplemented with 3 mM $ZnCl_2$ and incubated ~16 h at 19 °C. Crystals were then transferred into a cryo-protectant solution of the crystallization solution supplemented with both 1 mM $ZnCl_2$ and 20% glycerol and subsequently frozen in liquid nitrogen.

Diffraction images were collected at the Advanced Light Source beamline 5.0.2. Data were indexed, integrated, and scaled using XDS and XSCALE (53). Both structures were solved by molecular replacement with Phaser-MR within the Phenix package (54, 55), using the monomeric CARD11–CARD structure (PDB code 4LWD) as a search model for the apo structure and the apo domain-swapped dimer structure as a search model for the Zn^{2+}-bound structure. For both structures, iterative cycles of model building in COOT (56) and refinement in Phenix were used to generate final models. All structural depictions were generated in PyMOL.

Monomer–dimer interconversion kinetics

300 μM ^{15}N-labeled dimeric CARD9–CARD samples were generated in 50 mM HEPES, 300 mM NaCl, 500 μM $ZnCl_2$, 0.5 mM TCEP, pH 7.0, with or without 1 mM EDTA. Samples were transferred to 25 °C followed by immediate collection of SOFAST-HMQC (52) experiments at 25 °C on a Bruker 600-MHz spectrometer. Between time points, samples were incubated at 25 °C. For CARD11, 180 μM ^{15}N-labeled dimeric CARD11–CARD was prepared in 50 mM HEPES, 300 mM NaCl, 0.5 mM TCEP, pH 7.0; the sample was generated by concentrating fractions from the dimer peak in Fig. S4*A* at 4 °C for ~1 h, followed by immediate data collection at 25 °C. The mid-point of the SOFAST-HMQC experiments was used as the time points for both plotting and fitting. Monomeric and dimeric peak heights were fit simultaneously to a single-phase exponential for each sample using GraphPad Prism 7 using amide peak of Ser-28 (CARD9) or the peak boxed out in Fig. S4*B* (CARD11).

CARD9–CARD filament formation

Zn^{2+}-bound CARD9–CARD was prepared by saturating with Zn^{2+} prior to a final size-exclusion purification step. 50 μl of Zn^{2+}-bound CARD9–CARD was prepared in 50 mM Tris, 150 or 300 mM NaCl, 0.5 mM TCEP at the indicated concentrations in a 384-well clear-bottom plate. At $t = 0$, Zn^{2+} was removed by addition of 250 μM EDTA. Filament formation was monitored by measuring absorbance at 350 nm on a Molecular Devices SpectraMax M5e plate reader while shaking at 25 °C. At the indicated time point, an additional 250 μM $ZnCl_2$ was added to each well, and monitoring was continued. Samples for EM were taken just prior to EDTA addition, just prior to Zn^{2+} addition, and at the end of the assay.

Bcl10 fluorescence polarization assay

The assay was performed in a 20-μl volume in 20 mM Tris, 150 mM NaCl, 0.5 mM TCEP, pH 7.5, with 1 or 2 μM final concentration of MBP–Bcl10 as indicated. CARD9–CARD filaments were prepared as in Fig. 6*C* by addition of 250 μM EDTA to 200 μM Zn^{2+}-saturated CARD9–CARD, followed by incubation with shaking at 25 °C for 90 min. The CARD9–CARD monomer control was treated identically to the filament sample, but without addition of EDTA. At the initiation of the experiment, TEV protease was added to 0.05 mg/ml along with CARD9–CARD monomer or filaments as indicated. Fluorescence polarization was measured by exciting at 495 nm and monitoring at 519 nm on a Molecular Devices SpectraMax M5e plate reader at 25 °C. We note that by the 90-min end point of the FP assay at 25 °C, small numbers of filaments form in the MBP–Bcl10 sample in the absence of TEV, indicating that the MBP is not absolute in its ability to block polymerization (Fig. S5*D*). These filaments are sufficiently sparse as to not register on the FP assay (Fig. 6*E*) and much thicker than the Bcl10 filaments that form upon TEV cleavage, ensuring that we are not observing them in Fig. 6, *F* and *H*.

EM and helical reconstruction

Negative stain samples were generated by incubating on glow-discharged carbon on 400-mesh copper grids (Electron Microscopy Sciences) for 30 s, followed by staining with 2% uranyl acetate. For Fig. 6, *A* and *B*, and Fig. S5, *A* and *D*, and micrographs used for helical reconstruction of the CARD9–CARD filaments, 4-μl samples were applied at 200 μM with no dilution. For Fig. 6, *F* and *H*, samples were prepared by mixing MBP–Bcl10 (2 μM), CARD9–CARD filaments (10 μM), and/or TEV (0.05 mg/ml) as indicated and incubating at room temperature for 2 min followed by direct application of 4 μl onto the grid, with no dilution.

Grids were imaged using a Talos F200C microscope operated at 200 kV and Ceta camera (ThermoFisher Scientific). Images for helical reconstruction were collected at 2.006 Å/pixel; all other images were collected at 4.097 Å/pixel. For helical reconstruction of the CARD9–CARD filament, filaments were manually picked using the EMAN2 program e2helixboxer (57), and

all subsequent processing steps were performed utilizing routines in Spring (58). CTF parameters were determined using Micctfdetermine, which utilizes CTFFIND (59). Micrographs were CTF corrected and segmented using Segment, yielding 16,754 segments, which were classified into 50 classes using Segmentclass. Six of these classes (chosen by visual inspection) were analyzed using Segclassreconstruct, which computes a 3D reconstruction based on a single class average over a set of incremented helical symmetries (*i.e.* rise and rotation); the projections of these reconstructions are quantitatively compared against the original class average to identify helical symmetries compatible with the class average. Of those helical parameters that returned a high-correlation coefficient, the 3D reconstructions were visually inspected to identify structures that contained volumes compatible with the globular CARD9–CARD. These helical parameters were then used as an input to Segmentrefine3D to iteratively refine the structure from the segment stack, beginning from a cylinder of radius 100 Å. Finally, the 2D projections and power spectra of the reconstructions were compared against the class averages; only the reported parameters of a 5-Å rise and 102° rotation yielded a projection and power spectrum that matched the class averages (Fig. S6, *A–C*). The final reconstruction utilized 11,226 segments. Using six independent class averages, we ran Segclassreconstruct with fine spacing (0.1 Å and 0.1°) around 5 Å and 102°. The highest correlation symmetry parameters in all cases were within ± 0.1 Å and ± 0.5° of the reported symmetry, providing an estimate of the uncertainty in these values. Fourier shell correlation analysis (Fig. S6*D*) of the final structure indicates a resolution of 13.0 Å; however, we were unable to discern significant structural details beyond the location of the individual CARD9–CARDs, and so we suggest by comparison with other comparable structures that the resolution is ~20 Å.

Sequence alignment

Multiple sequence alignments were performed using Clustal Omega (60).

Author contributions—M. J. H., E. H., A. R., E. C. D., and W. J. F. conceptualization; M. J. H. data curation; M. J. H., R. F., and A. R. formal analysis; M. J. H. validation; M. J. H., R. F., G. d. L. B., A. E., and A. R. investigation; M. J. H. visualization; M. J. H., A. R., E. C. D., and W. J. F. methodology; M. J. H. writing-original draft; M. J. H., E. H., A. R., E. C. D., and W. J. F. writing-review and editing; A. R., E. C. D., and W. J. F. supervision.

Acknowledgments—We thank Menno van Lookeren Campagne, Joseph Chavarria-Smith, Erik Verschueren, and Peter Liu for their helpful discussions and assistance in this study. We thank Hao Wu (Harvard University) for assistance with the Bcl10 fluorescence polarization assay.

References

1. Taylor, P. R., Tsoni, S. V., Willment, J. A., Dennehy, K. M., Rosas, M., Findon, H., Haynes, K., Steele, C., Botto, M., Gordon, S., and Brown, G. D. (2007) Dectin-1 is required for β-glucan recognition and control of fungal infection. *Nat. Immunol.* **8,** 31–38 CrossRef Medline
2. Wells, C. A., Salvage-Jones, J. A., Li, X., Hitchens, K., Butcher, S., Murray, R. Z., Beckhouse, A. G., Lo, Y. L., Manzanero, S., Cobbold, C., Schroder, K., Ma, B., Orr, S., Stewart, L., Lebus, D., *et al.* (2008) The macrophage-inducible C-type lectin, mincle, is an essential component of the innate immune response to *Candida albicans*. *J. Immunol.* **180,** 7404–7413 CrossRef Medline
3. Robinson, M. J., Osorio, F., Rosas, M., Freitas, R. P., Schweighoffer, E., Gross, O., Verbeek, J. S., Ruland, J., Tybulewicz, V., Brown, G. D., Moita, L. F., Taylor, P. R., and Reis e Sousa, C. (2009) Dectin-2 is a Syk-coupled pattern recognition receptor crucial for Th17 responses to fungal infection. *J. Exp. Med.* **206,** 2037–2051 CrossRef Medline
4. Gross, O., Gewies, A., Finger, K., Schäfer, M., Sparwasser, T., Peschel, C., Förster, I., and Ruland, J. (2006) Card9 controls a non-TLR signalling pathway for innate anti-fungal immunity. *Nature* **442,** 651–656 CrossRef Medline
5. Strasser, D., Neumann, K., Bergmann, H., Marakalala, M. J., Guler, R., Rojowska, A., Hopfner, K. P., Brombacher, F., Urlaub, H., Baier, G., Brown, G. D., Leitges, M., and Ruland, J. (2012) Syk kinase-coupled C-type lectin receptors engage protein kinase C-σ to elicit Card9 adaptor-mediated innate immunity. *Immunity* **36,** 32–42 CrossRef Medline
6. Bertin, J., Guo, Y., Wang, L., Srinivasula, S. M., Jacobson, M. D., Poyet, J. L., Merriam, S., Du, M. Q., Dyer, M. J., Robison, K. E., DiStefano, P. S., and Alnemri, E. S. (2000) CARD9 is a novel caspase recruitment domain-containing protein that interacts with BCL10/CLAP and activates NF-κB. *J. Biol. Chem.* **275,** 41082–41086 CrossRef Medline
7. Lanternier, F., Pathan, S., Vincent, Q. B., Liu, L., Cypowyj, S., Prando, C., Migaud, M., Taibi, L., Ammar-Khodja, A., Stambouli, O. B., Guellil, B., Jacobs, F., Goffard, J. C., Schepers, K., Del Marmol, V., *et al.* (2013) Deep dermatophytosis and inherited CARD9 deficiency. *N. Engl. J. Med.* **369,** 1704–1714 CrossRef Medline
8. Lanternier, F., Mahdaviani, S. A., Barbati, E., Chaussade, H., Koumar, Y., Levy, R., Denis, B., Brunel, A. S., Martin, S., Loop, M., Peeters, J., de Selys, A., Vanclaire, J., Vermylen, C., Nassogne, M. C., *et al.* (2015) Inherited CARD9 deficiency in otherwise healthy children and adults with *Candida* species-induced meningoencephalitis, colitis, or both. *J. Allergy Clin. Immunol.* **135,** 1558–1568.e2 CrossRef Medline
9. Rieber, N., Gazendam, R. P., Freeman, A. F., Hsu, A. P., Collar, A. L., Sugui, J. A., Drummond, R. A., Rongkavilit, C., Hoffman, K., Henderson, C., Clark, L., Mezger, M., Swamydas, M., Engeholm, M., Schüle, R., *et al.* (2016) Extrapulmonary *Aspergillus* infection in patients with CARD9 deficiency. *JCI Insight* **1,** e89890 Medline
10. Glocker, E. O., Hennigs, A., Nabavi, M., Schäffer, A. A., Woellner, C., Salzer, U., Pfeifer, D., Veelken, H., Warnatz, K., Tahami, F., Jamal, S., Manguiat, A., Rezaei, N., Amirzargar, A. A., Plebani, A., *et al.* (2009) A homozygous CARD9 mutation in a family with susceptibility to fungal infections. *N. Engl. J. Med.* **361,** 1727–1735 CrossRef Medline
11. Roth, S., Rottach, A., Lotz-Havla, A. S., Laux, V., Muschaweckh, A., Gersting, S. W., Muntau, A. C., Hopfner, K. P., Jin, L., Vanness, K., Petrini, J. H., Drexler, I., Leonhardt, H., and Ruland, J. (2014) Rad50-CARD9 interactions link cytosolic DNA sensing to IL-1β production. *Nat. Immunol.* **15,** 538–545 CrossRef Medline
12. Hsu, Y. M., Zhang, Y., You, Y., Wang, D., Li, H., Duramad, O., Qin, X. F., Dong, C., and Lin, X. (2007) The adaptor protein CARD9 is required for innate immune responses to intracellular pathogens. *Nat. Immunol.* **8,** 198–205 CrossRef Medline
13. Poeck, H., Bscheider, M., Gross, O., Finger, K., Roth, S., Rebsamen, M., Hannesschläger, N., Schlee, M., Rothenfusser, S., Barchet, W., Kato, H., Akira, S., Inoue, S., Endres, S., Peschel, C., *et al.* (2010) Recognition of RNA virus by RIG-I results in activation of CARD9 and inflammasome signaling for interleukin 1β production. *Nat. Immunol.* **11,** 63–69 CrossRef Medline
14. Zhernakova, A., Festen, E. M., Franke, L., Trynka, G., van Diemen, C. C., Monsuur, A. J., Bevova, M., Nijmeijer, R. M., van 't Slot, R., Heijmans, R., Boezen, H. M., van Heel, D. A., van Bodegraven, A. A., Stokkers, P. C., Wijmenga, C., *et al.* (2008) Genetic analysis of innate immunity in Crohn's disease and ulcerative colitis identifies two susceptibility loci harboring CARD9 and IL18RAP. *Am. J. Hum. Genet.* **82,** 1202–1210 CrossRef Medline
15. Hong, S. N., Park, C., Park, S. J., Lee, C. K., Ye, B. D., Kim, Y. S., Lee, S., Chae, J., Kim, J. I., Kim, Y. H., and IBD Study Group of the Korean Asso-

ciation for the Study of Intestinal Diseases (KASID)). (2016) Deep resequencing of 131 Crohn's disease associated genes in pooled DNA confirmed three reported variants and identified eight novel variants. *Gut* **65,** 788–796 CrossRef Medline

16. Lee, E. J., Brown, B. R., Vance, E. E., Snow, P. E., Silver, P. B., Heinrichs, D., Lin, X., Iwakura, Y., Wells, C. A., Caspi, R. R., and Rosenzweig, H. L. (2016) Mincle activation and the Syk/Card9 signaling axis are central to the development of autoimmune disease of the eye. *J. Immunol.* **196,** 3148–3158 CrossRef Medline
17. Peterson, M. R., Haller, S. E., Ren, J., Nair, S., and He, G. (2016) CARD9 as a potential target in cardiovascular disease. *Drug Des. Devel. Ther.* **10,** 3799–3804 CrossRef Medline
18. Wang, S., Gu, J., Xu, Z., Zhang, Z., Bai, T., Xu, J., Cai, J., Barnes, G., Liu, Q. J., Freedman, J. H., Wang, Y., Liu, Q., Zheng, Y., and Cai, L. (2017) Zinc rescues obesity-induced cardiac hypertrophy via stimulating metallothionein to suppress oxidative stress-activated BCL10/CARD9/p38 MAPK pathway. *J. Cell. Mol. Med.* **21,** 1182–1192 CrossRef Medline
19. Haase, H., Ober-Blöbaum, J. L., Engelhardt, G., Hebel, S., Heit, A., Heine, H., and Rink, L. (2008) Zinc signals are essential for lipopolysaccharide-induced signal transduction in monocytes. *J. Immunol.* **181,** 6491–6502 CrossRef Medline
20. Yamasaki, S., Sakata-Sogawa, K., Hasegawa, A., Suzuki, T., Kabu, K., Sato, E., Kurosaki, T., Yamashita, S., Tokunaga, M., Nishida, K., and Hirano, T. (2007) Zinc is a novel intracellular second messenger. *J. Cell Biol.* **177,** 637–645 CrossRef Medline
21. Hojyo, S., and Fukada, T. (2016) Roles of zinc signaling in the immune system. *J. Immunol. Res.* 2016, 6762343 Medline
22. Haase, H., and Rink, L. (2009) Functional significance of zinc-related signaling pathways in immune cells. *Annu. Rev. Nutr.* **29,** 133–152 CrossRef Medline
23. Qiao, Q., Yang, C., Zheng, C., Fontán, L., David, L., Yu, X., Bracken, C., Rosen, M., Melnick, A., Egelman, E. H., and Wu, H. (2013) Structural architecture of the CARMA1/Bcl10/MALT1 signalosome: nucleation-induced filamentous assembly. *Mol. Cell* **51,** 766–779 CrossRef Medline
24. Irving, H., and Williams, R. J. (1953) The stability of transition-metal complexes. *J. Chem. Soc.* 3192–3210 CrossRef
25. Rae, T. D., Schmidt, P. J., Pufahl, R. A., Culotta, V. C., and O'Halloran, T. V. (1999) Undetectable intracellular free copper: the requirement of a copper chaperone for superoxide dismutase. *Science* **284,** 805–808 CrossRef Medline
26. McCranor, B. J., Szmacinski, H., Zeng, H. H., Stoddard, A. K., Hurst, T., Fierke, C. A., Lakowicz, J. R., and Thompson, R. B. (2014) Fluorescence lifetime imaging of physiological free Cu(II) levels in live cells with a Cu(II)-selective carbonic anhydrase-based biosensor. *Metallomics* **6,** 1034–1042 CrossRef Medline
27. Simons, T. J. (1993) Measurement of free Zn^{2+} ion concentration with the fluorescent probe mag-fura-2 (furaptra). *J Biochem Biophys Methods* **27,** 25–37 CrossRef Medline
28. Wang, Z. X. (1995) An exact mathematical expression for describing competitive binding of two different ligands to a protein molecule. *FEBS Lett.* **360,** 111–114 CrossRef Medline
29. Jefferson, J. R., Hunt, J. B., and Ginsburg, A. (1990) Characterization of indo-1 and quin-2 as spectroscopic probes for Zn^{2+}–protein interactions. *Anal. Biochem.* **187,** 328–336 CrossRef Medline
30. David, L., Li, Y., Ma, J., Garner, E., Zhang, X., and Wu, H. (2018) Assembly mechanism of the CARMA1-BCL10-MALT1-TRAF6 signalosome. *Proc. Natl. Acad. Sci. U.S.A.* **115,** 1499–1504 CrossRef Medline
31. Maret, W. (2013) Zinc biochemistry: from a single zinc enzyme to a key element of life. *Adv. Nutr.* **4,** 82–91 CrossRef Medline
32. Andreini, C., Banci, L., Bertini, I., and Rosato, A. (2006) Counting the zinc-proteins encoded in the human genome. *J. Proteome Res.* **5,** 196–201 CrossRef Medline
33. Bozym, R. A., Thompson, R. B., Stoddard, A. K., and Fierke, C. A. (2006) Measuring picomolar intracellular exchangeable zinc in PC-12 cells using a ratiometric fluorescence biosensor. *ACS Chem. Biol.* **1,** 103–111 CrossRef Medline
34. Li, Y., and Maret, W. (2009) Transient fluctuations of intracellular zinc ions in cell proliferation. *Exp. Cell Res.* **315,** 2463–2470 CrossRef Medline
35. Vinkenborg, J. L., Nicolson, T. J., Bellomo, E. A., Koay, M. S., Rutter, G. A., and Merkx, M. (2009) Genetically encoded FRET sensors to monitor intracellular Zn^{2+} homeostasis. *Nat. Methods* **6,** 737–740 CrossRef Medline
36. Krezel, A., and Maret, W. (2006) Zinc-buffering capacity of a eukaryotic cell at physiological pZn. *J. Biol. Inorg. Chem.* **11,** 1049–1062 CrossRef Medline
37. Hessels, A. M., Chabosseau, P., Bakker, M. H., Engelen, W., Rutter, G. A., Taylor, K. M., and Merkx, M. (2015) eZinCh-2: a versatile, genetically encoded FRET sensor for cytosolic and intraorganelle Zn^{2+} imaging. *ACS Chem. Biol.* **10,** 2126–2134 CrossRef Medline
38. Adebodun, F., and Post, J. F. (1995) Role of intracellular free Ca(II) and Zn(II) in dexamethasone-induced apoptosis and dexamethasone resistance in human leukemic CEM cell lines. *J. Cell. Physiol.* **163,** 80–86 CrossRef Medline
39. Peck, E. J., Jr., and Ray, W. J., Jr. (1971) Metal complexes of phosphoglucomutase *in vivo*. Alterations induced by insulin. *J. Biol. Chem.* **246,** 1160–1167 Medline
40. Qin, Y., Miranda, J. G., Stoddard, C. I., Dean, K. M., Galati, D. F., and Palmer, A. E. (2013) Direct comparison of a genetically encoded sensor and small molecule indicator: implications for quantification of cytosolic Zn^{2+}. *ACS Chem. Biol.* **8,** 2366–2371 CrossRef Medline
41. Bafaro, E., Liu, Y., Xu, Y., and Dempski, R. E. (2017) The emerging role of zinc transporters in cellular homeostasis and cancer. *Signal. Transduct. Target Ther.* **2,** 17029 CrossRef Medline
42. Kitamura, H., Morikawa, H., Kamon, H., Iguchi, M., Hojyo, S., Fukada, T., Yamashita, S., Kaisho, T., Akira, S., Murakami, M., and Hirano, T. (2006) Toll-like receptor-mediated regulation of zinc homeostasis influences dendritic cell function. *Nat. Immunol.* **7,** 971–977 CrossRef Medline
43. Ferrao, R., and Wu, H. (2012) Helical assembly in the death domain (DD) superfamily. *Curr. Opin. Struct. Biol.* **22,** 241–247 CrossRef Medline
44. Studier, F. W. (2005) Protein production by auto-induction in high density shaking cultures. *Protein Expr. Purif.* **41,** 207–234 CrossRef Medline
45. Senn, H., Werner, B., Messerle, B. A., Weber, C., Traber, R., and Wuthrich, K. (1989) Stereospecific assignment of the methyl H-1-NMR lines of valine and leucine in polypeptides by nonrandom C-13 labeling. *FEBS Lett.* **249,** 113–118 CrossRef
46. Vranken, W. F., Boucher, W., Stevens, T. J., Fogh, R. H., Pajon, A., Llinas, M., Ulrich, E. L., Markley, J. L., Ionides, J., and Laue, E. D. (2005) The CCPN data model for NMR spectroscopy: development of a software pipeline. *Proteins* **59,** 687–696 CrossRef Medline
47. Shen, Y., Delaglio, F., Cornilescu, G., and Bax, A. (2009) TALOS+: a hybrid method for predicting protein backbone torsion angles from NMR chemical shifts. *J Biomol NMR* **44,** 213–223 CrossRef Medline
48. Güntert, P., Mumenthaler, C., and Wüthrich, K. (1997) Torsion angle dynamics for NMR structure calculation with the new program DYANA. *J. Mol. Biol.* **273,** 283–298 CrossRef Medline
49. Herrmann, T., Güntert, P., and Wüthrich, K. (2002) Protein NMR structure determination with automated NOE assignment using the new software CANDID and the torsion angle dynamics algorithm DYANA. *J. Mol. Biol.* **319,** 209–227 CrossRef Medline
50. Brünger, A. T., Adams, P. D., Clore, G. M., DeLano, W. L., Gros, P., Grosse-Kunstleve, R. W., Jiang, J. S., Kuszewski, J., Nilges, M., Pannu, N. S., Read, R. J., Rice, L. M., Simonson, T., and Warren, G. L. (1998) Crystallography and NMR system: a new software suite for macromolecular structure determination. *Acta Crystallogr. D Biol. Crystallogr.* **54,** 905–921 CrossRef Medline
51. Brunger, A. T. (2007) Version 1.2 of the Crystallography and NMR system. *Nat. Protoc.* **2,** 2728–2733 CrossRef Medline
52. Schanda, P., Kupce, E., and Brutscher, B. (2005) SOFAST-HMQC experiments for recording two-dimensional heteronuclear correlation spectra of proteins within a few seconds. *J. Biomol. NMR* **33,** 199–211 CrossRef Medline
53. Kabsch, W. (2010) XDS. *Acta Crystallogr. D Biol. Crystallogr.* **66,** 125–132 CrossRef Medline
54. McCoy, A. J. (2007) Solving structures of protein complexes by molecular replacement with Phaser. *Acta Crystallogr. D Biol. Crystallogr.* **63,** 32–41 CrossRef Medline

55. Adams, P. D., Afonine, P. V., Bunkóczi, G., Chen, V. B., Davis, I. W., Echols, N., Headd, J. J., Hung, L. W., Kapral, G. J., Grosse-Kunstleve, R. W., McCoy, A. J., Moriarty, N. W., Oeffner, R., Read, R. J., Richardson, D. C., *et al.* (2010) PHENIX: a comprehensive Python-based system for macromolecular structure solution. *Acta Crystallogr. D Biol. Crystallogr.* **66,** 213–221 CrossRef Medline
56. Emsley, P., and Cowtan, K. (2004) Coot: model-building tools for molecular graphics. *Acta Crystallogr. D Biol. Crystallogr.* **60,** 2126–2132 CrossRef Medline
57. Tang, G., Peng, L., Baldwin, P. R., Mann, D. S., Jiang, W., Rees, I., and Ludtke, S. J. (2007) EMAN2: an extensible image processing suite for electron microscopy. *J. Struct. Biol.* **157,** 38–46 CrossRef Medline
58. Desfosses, A., Ciuffa, R., Gutsche, I., and Sachse, C. (2014) SPRING-an image processing package for single-particle based helical reconstruction from electron cryomicrographs. *J. Struct. Biol.* **185,** 15–26 CrossRef Medline
59. Mindell, J. A., and Grigorieff, N. (2003) Accurate determination of local defocus and specimen tilt in electron microscopy. *J. Struct. Biol.* **142,** 334–347 CrossRef Medline
60. Sievers, F., Wilm, A., Dineen, D., Gibson, T. J., Karplus, K., Li, W., Lopez, R., McWilliam, H., Remmert, M., Söding, J., Thompson, J. D., and Higgins, D. G. (2011) Fast, scalable generation of high-quality protein multiple sequence alignments using Clustal Omega. *Mol. Syst. Biol.* **7,** 539 Medline